



## Experimental study on flame shape characteristics of CH<sub>4</sub> combustor under exhaust gas aspiration

Jeong Won Kim<sup>1</sup> · Juwon Park<sup>2,3</sup> · Sung Hwan Yoon<sup>†</sup>

(Received February 12, 2025 : Revised February 17, 2025 : Accepted February 24, 2025)

**Abstract:** The International Energy Agency (IEA) reports that global carbon dioxide emissions continue to rise, particularly in developing regions with high fossil fuel reliance. Although liquefied natural gas (LNG) is recognized as a transitional energy source due to its lower CO<sub>2</sub> emissions compared to coal and oil, its primary component, methane, exhibits a high global warming potential and still generates significant air pollutants—such as CO<sub>2</sub>, CO, and NO<sub>x</sub>—during combustion. Moreover, combustion emissions from indoor appliances, such as household gas stoves, pose serious health risks to users; in enclosed spaces, the accumulation of carbon monoxide can lead to fatal poisoning. This study experimentally investigates methane combustion efficiency using nitrogen-diluted methane diffusion flames with aspiration technology to reduce harmful emissions. A coaxial flow burner connected to a vacuum pump was used to examine diffusion flame formation under varying fuel dilution ratios, suction flow rates, and nozzle injection conditions. A total of 87 gas mixtures were tested, and the resulting flame structures were classified into five regimes (Regime I to Regime V). As the suction flow rate increased, the flame transitioned from Regime I to Regime V. Moreover, as the conditions approached Regime V, the volume fraction of soot within the flame decreased, and the flame exhibited luminosity similar to that of blue, premixed flames. The successful characterization of flame lengths under various gas conditions provides valuable insights for optimizing industrial combustor designs.

**Keywords:** Methane, Diffusion flame, Co-axial, Exhaust gas, Aspiration

### 1. Introduction

The history of global environmental policies dates back to the 1992 United Nations Framework Convention on Climate Change (UNFCCC), which served as a foundational international agreement addressing climate change. According to this declaration, signatory nations were required to implement national policies for reducing greenhouse gas (GHG) emissions in accordance with their respective circumstances and to compile national statistics on GHG emissions and absorption levels [1]. Subsequently, the Kyoto Protocol, established in 1997, legally mandated emission reduction obligations for 37 countries, including Australia, Canada, the United States, Japan, and European Union member states. This protocol, which came into effect in 2005, targeted the reduction of six major greenhouse gases: carbon

dioxide (CO<sub>2</sub>), methane (CH<sub>4</sub>), nitrous oxide (N<sub>2</sub>O), perfluorocarbons (PFCs), hydrofluorocarbons (HFCs), and sulfur hexafluoride (SF<sub>6</sub>) [2]-[5].

To replace the Kyoto Protocol, which expired in 2020, the Paris Agreement was adopted in 2015 as a universal framework for climate action, involving all nations. The agreement aimed to limit global temperature rise to below 2°C, with efforts to further restrict it to 1.5°C [6][7]. To achieve these goals, global GHG emissions must be reduced by at least 45% from 2010 levels by 2030, with the ultimate objective of achieving carbon neutrality by 2050 [8]-[11]. International efforts to address environmental issues have been emphasized in response to the severe environmental degradation caused by industrialization and economic growth. However, according to the International Energy

<sup>†</sup> Corresponding Author (ORCID: <https://orcid.org/0000-0001-5794-3286>): Associate Professor, Department of Marine System Engineering, Korea Maritime & Ocean University, 727, Taejong-ro, Yeongdo-gu, Busan 49112, Korea, E-mail: shy@kmou.ac.kr, Tel: +51-410-4261

1 M. S. Candidate, Department of green and smart ship equipment, National Korea Maritime & Ocean University, E-mail: eit9983@eit-one.com, Tel: +82-70-4121-0633

2 Ph. D. Candidate, Department of Marine System Engineering, National Korea Maritime & Ocean University, E-mail: pjw6642@g.kmou.ac.kr, Tel: +82-51-410-4261

3 Ph. D. Candidate, Interdisciplinary Major of Maritime AI Convergence, National Korea Maritime & Ocean University, E-mail: pjw6642@g.kmou.ac.kr, Tel: +82-51-410-4261

This is an Open Access article distributed under the terms of the Creative Commons Attribution Non-Commercial License (<http://creativecommons.org/licenses/by-nc/3.0>), which permits unrestricted non-commercial use, distribution, and reproduction in any medium, provided the original work is properly cited.

Agency's (IEA) CO<sub>2</sub> Emissions in 2022 report, global CO<sub>2</sub> emissions increased in some countries following the COVID-19 pandemic due to rising energy demand in industrial and transportation sectors. This trend is particularly evident in developing and emerging economies, where rapid industrialization and urbanization have led to increased energy consumption. Although renewable energy should ideally be prioritized, cost constraints have resulted in continued reliance on fossil fuels such as coal, oil, and natural gas [12].

While the ultimate solution for GHG emission reduction is a complete transition to renewable energy, the financial and logistical challenges associated with this transition suggest that it will take considerable time. Consequently, the role of bridge fuels has gained attention as a transitional solution [13][14]. Among these, liquefied natural gas (LNG) is recognized for its environmental benefits, emitting less CO<sub>2</sub> than coal or oil while producing minimal particulate matter and sulfur oxides during combustion. Additionally, LNG offers economic advantages by utilizing existing infrastructure and facilitating easier transportation and storage, making it a viable short-term solution for reducing fossil fuel dependence. LNG has been particularly highlighted as an effective alternative for reducing carbon emissions in the maritime and power generation sectors. In response to the International Maritime Organization's (IMO) tightened emission regulations, many shipping operators have adopted LNG propulsion systems, which produce lower carbon emissions than conventional heavy fuel oil (HFO). Furthermore, LNG combustion significantly reduces soot and fine particulate matter emissions, contributing to improved air quality.

However, methane, the primary component of LNG, is one of the six major greenhouse gases and is a key contributor to climate change. Methane exhibits a much higher global warming potential (GWP) than CO<sub>2</sub> over short periods. According to the Intergovernmental Panel on Climate Change (IPCC) 2021 Report, methane has a GWP approximately 29 times that of CO<sub>2</sub> over a 100-year period and up to 82 times over a 20-year period [15][16]. This highlights the significant short-term impact of methane on global warming [17]. In particular, the issue of methane slip resulting from incomplete combustion remains a significant concern. Given that methane possesses a substantially higher global warming potential (GWP) than carbon dioxide over a short timescale, addressing methane emissions is crucial. Extensive research is essential, including the development of advanced

post-combustion treatment technologies and catalytic systems to mitigate methane emissions released into the atmosphere due to methane slip. In addition, the increasing atmospheric concentration of methane is a critical climate factor, necessitating effective research and monitoring for its management.

Methane comprises approximately 70–90% of LNG by volume and serves as an economically efficient and effective energy source, particularly in household applications. Gas stoves, in particular, are widely used due to their convenience and cost-effectiveness [20]. However, the combustion process of gas stoves produces various by-products that can negatively impact indoor air quality, posing potential health and environmental risks. In particular, the use of gas stoves in enclosed environments can lead to the accumulation of harmful combustion by-products, posing a significant threat to user health and, in severe cases, may result in fatal carbon monoxide poisoning. Therefore, in South Korea, national standards from the Korean Agency for Technology and Standards (KATS) require the installation of range hoods for gas stoves [21]. However, due to the spatial separation between the stove and the ventilation system, complete gas capture is not always achieved.

To address this issue, our research team aims to enhance conventional gas stove combustion by incorporating aspiration technology, providing a more environmentally friendly solution to methane combustion.

## 2. Experimental method

### 2.1 Experimental Method

This study applied a coaxial burner configuration, commonly known as the Santoro burner. **Figure 1** presents a schematic diagram of the detailed setup of the coaxial burner, while **Figure 2** illustrates the overall aspiration technology used in the experiment. The burner body was constructed from stainless steel with a diameter of 100 mm, and a stainless steel tube with an outer diameter of 5 mm and an inner diameter of 3.8 mm was integrated at the center to define the nozzle specifications. To ensure uniform coaxial suction flow, four ports were placed at a 90-degree angle at the lower section of the burner body. To enhance the uniformity of suction flow within the burner, 3 mm-diameter glass beads were placed at the bottom, followed by a 70 mm-thick ceramic honeycomb with 1 mm-spaced square channels. This design ensured even flow distribution as the fluid passed through

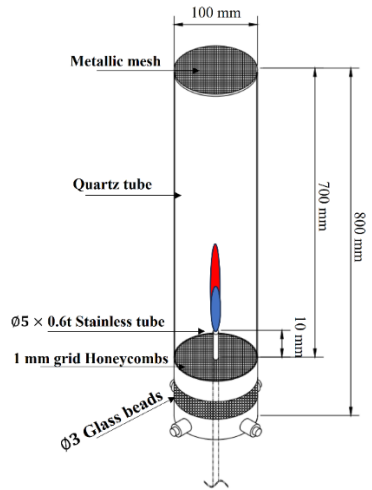


**Figure 1:** Co-axial burner detail setup

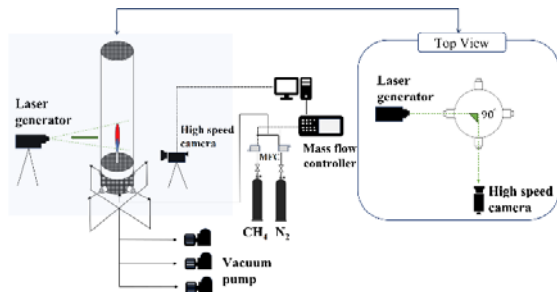


**Figure 2:** Experimental for evaluating suction capacity

the voids between the glass beads and ceramic honeycomb channels. The protrusion height of the stainless steel nozzle was experimentally validated through multiple trials to achieve a stable diffusion flame, and the final protrusion height was set at 10 mm.

To minimize instability caused by external flow, a quartz tube (100 mm in diameter, 700 mm in height) was installed above the coaxial burner. A fine metal mesh was attached to the upper part of the quartz tube to ensure the uniformity of oxygen flow. The fuel used in this study was 99.5% pure methane, and 99.9% pure nitrogen was used as a diluent for different dilution ratios. Gas flow rates were precisely controlled using MFC controller(ATO-VAC GMC 1200) and mass flow controller(ATO-VAC AFC 500 MFC), with calibration performed using a calibrator(Mesa Labs Defender 530+H) to ensure accurate gas mixtures. Due to the dependency of the mass flow controller's accuracy on ambient temperature, the device was calibrated with a calibrator prior to each experimental run to ensure precise flow control. The fuel injection line utilized polyurethane tubing (O.D. : 6 mm, I.D. : 4 mm), and to provide sufficient dilution volume, two tubes were merged, maintaining a total length of over 1 meter before reaching the nozzle outlet. The suction line was connected to a vacuum

pump using polyurethane tubing (O.D. : 12 mm, I.D. : 8 mm) to ensure adequate suction flow.

To extract emissions, three vacuum pumps were used, each with a coaxial aspiration velocity of  $-20$  cm/s. As illustrated in Figure 2, the coaxial aspiration velocity under vacuum pump operation was analyzed using Particle Image Velocimetry (PIV) with Mie scattering techniques. The dynamic behavior of the flow field was captured using a high-speed camera (Photron, Fastcam SA3) with a resolution of  $768 \times 1024$  pixels at 250 fps. Mie scattering was employed for visualization by seeding the fuel nozzle with TiO<sub>2</sub> particles ( $\sim 0.3$   $\mu\text{m}$ , LaVision). A 532 nm diode laser (GL-F-532) was used to illuminate the seed particles, forming a planar sheet beam in the flame zone through a combination of cylindrical and convex lenses. High-speed images of the flow field were recorded at 1000 fps and subsequently analyzed with an open-source MATLAB code to measure the velocity fields. An interrogation window was selected to have at least 15–25 particles, and the average particle displacement did not exceed 20% of the window size. Additionally, to maintain uniform coaxial aspiration velocity within different regions of the coaxial burner, a cross elbow fitting was used to pre-merge the piping, ensuring equal suction flow distribution across the four ports. All experimental conditions were recorded for at least 10 seconds using optical camcorder(SONY HDR-PJ675) connected to a PC, capturing video at 60 frames per second (fps). This video data was later processed using MATLAB for flame height measurement and Fast Fourier Transform (FFT) analysis. Given that recording at 60 fps for 10 seconds yielded a total of 600 images, and considering that FFT analysis requires the number of data points to be a power of 2, we arbitrarily selected 512 consecutive images for the FFT. The flame height was extracted from each image to construct a time-series dataset, which was then analyzed via FFT to determine the dominant oscillation frequencies and characterize the dynamic behavior of the flame with high precision.

## 2.2 Experimental Conditions

A total of 80 experimental conditions were evaluated by varying the following three parameters: methane-nitrogen dilution ratio, flow velocity of the gas mixture, and suction flow rate of the vacuum pump, as listed in **Table 1**. The methane-nitrogen ratio was adjusted to include fuel-rich and fuel-lean conditions under the baseline (no vacuum pump operation) scenario. Three different fuel mixture compositions were tested: 100% methane : 0% nitrogen, 50% methane : 50% nitrogen, and 40% methane : 60%

**Table 1:** Experimental conditions

Mix.	$X_f$ (Fuel mole fraction)		$U_{co}$ [cm/s]	$U_f$ [cm/s]
	CH <sub>4</sub>	N <sub>2</sub>		
1	1.0	0.0	0	20–180
2	0.5	0.5	–40	20–240
3	0.4	0.60	–60	20–120

nitrogen. The reason for diluting with nitrogen was to experimentally validate the effect of the suction flow technology across a wide range of combustion conditions, from commercial combustors that generate significant soot during combustion to domestic burners where oxygen is partially premixed due to the Venturi effect in the natural gas connection. According to the previous experimental results [22], nitrogen dilution progressively reduces soot formation due to its dilution effect. Therefore, by employing various nitrogen dilution ratios, we aimed to experimentally observe the additional effects of the suction flow technology under both high and low soot formation conditions.

The vacuum pump was configured to operate under three suction flow conditions: Baseline (free jet condition, no vacuum pump operation), –40 cm/s (two vacuum pumps in operation), and –60 cm/s (three vacuum pumps in operation). In the case of coaxial aspiration velocity (–40 cm/s, –60 cm/s), we utilized TiO<sub>2</sub> particles to measure the velocity of particle suction into the system. The total chamber length is 700 mm, and we recorded the velocity at the point where the TiO<sub>2</sub> particles reached the midpoint of the chamber (350 mm). When using two vacuum pumps, the measured velocity was 40 cm/s, whereas using all three vacuum pumps resulted in a measured velocity of 60 cm/s. This defines the coaxial aspiration velocity. The fuel velocity range ( $U_f$ ) was determined based on the condition where either the lifted flame reached the upper limit of the quartz pipe, or the fuel supply was insufficient to sustain combustion.

The flame structure and emission extraction behavior under different vacuum pump conditions were analyzed frame by frame using video recordings from a digital optical camcorder. The flame analysis was conducted using MATLAB, where the flame regimes were classified based on their dynamic behavior. Before MATLAB analysis, high-resolution video footage of the entire flame region was recorded. The video was then processed into individual frames, and flame height variation over time was quantitatively analyzed by measuring the highest pixel location of the flame boundary based on brightness contrast. Following the experiments, the flame structures were classified into different regimes, and a stability map analysis was conducted to

identify each regime's operational range. Furthermore, MATLAB (R2024b) was used to measure average flame height under different coaxial aspiration velocities. The Fast Fourier Transform (FFT) method was applied to analyze flame oscillation frequencies, allowing for an assessment of flame stability.

### 3. Result and Discussion

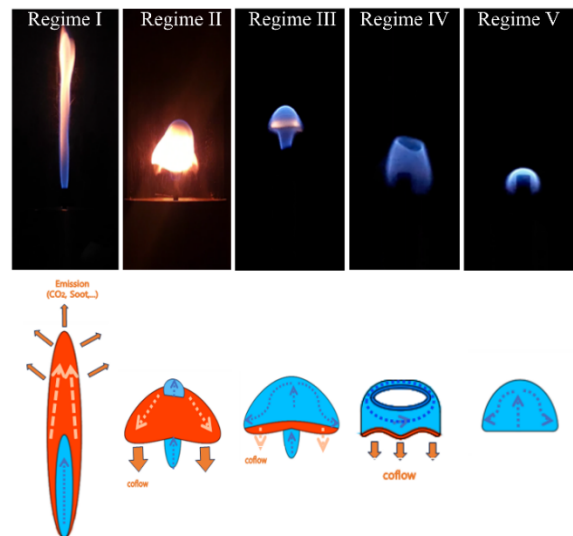
#### 3.1 Flame Formation Structure and Stability map

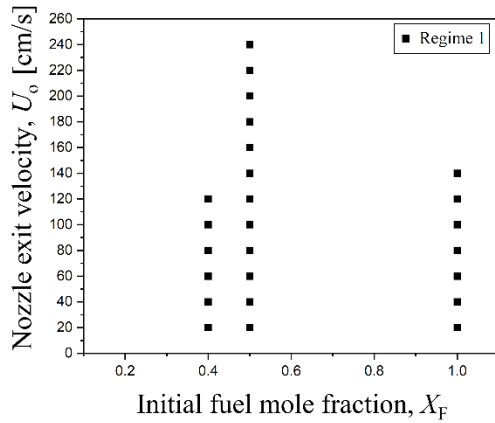
In this study, various flame structures were observed by setting CH<sub>4</sub>-N<sub>2</sub> dilution ratio, nozzle exit mean velocity, and coaxial aspiration velocity as variables. The observed flame structures were classified into five regimes, as shown in **Figure 3**.

In **Figure 3**, a decreasing trend in soot formation is observed from Regime I to V. Regime I represents a typical diffusion flame structure, displaying a velocity profile similar to typically the jet similarity solution.

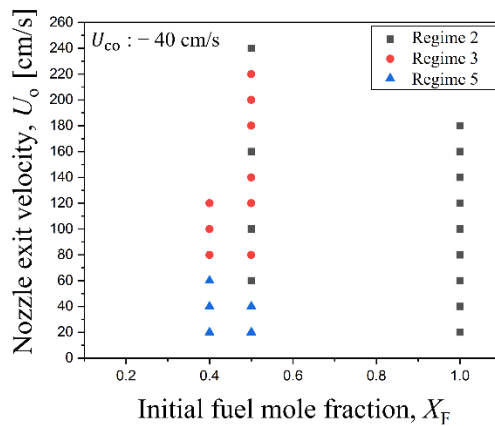
When suction flow is induced through the coaxial tube via a vacuum pump in a fundamental diffusion flame, a stagnation plane forms at the upper region of the flame. This leads to a reversal in the soot flow direction, where soot is redirected outward and downward, as depicted in Regime II. Visually, Regime II exhibits less soot compared to Regime I.

In Regime III and IV, soot formation is observed to be minimal, while in Regime V, the flame appears as a small, spherical shape at the nozzle tip, resembling a microgravity flame structure. The flames in Regime III–V commonly exhibit characteristics similar to a nearly partial premixed flame due to the combined effects of nitrogen dilution and oxygen entrainment.

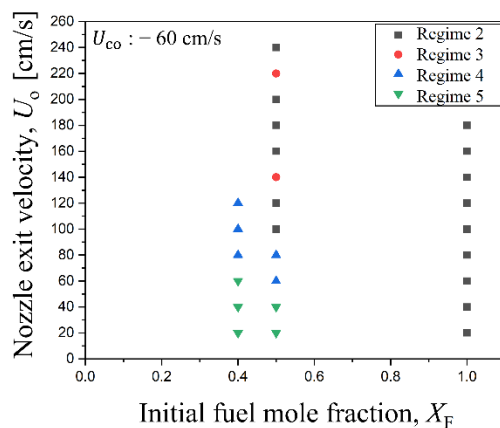
**Figure 3:** Flame formation structure(Regime I-V)



(a)



(b)



(c)

**Figure 4:** Stability maps representing the relationship between initial fuel mole fraction and nozzle exit mean velocity under varying coaxial aspiration velocities: (a)  $U_{co} = 0$  cm/s, (b)  $U_{co} = -40$  cm/s, and (c)  $U_{co} = -60$  cm/s

First, each regime was represented as a stability map based on flame shape, height, and emission characteristics, as illustrated in **Figure 4**. The stability map visualizes the relationship between fuel dilution ratio and nozzle exit mean velocity, while also

showing the distribution of flame regimes under different coaxial aspiration velocity conditions. **Figure 4(a)** corresponds to the condition without coaxial aspiration velocity ( $= 0$  cm/s). In a total of 25 experiments, all conditions exhibited a baseline diffusion flame structure, which was classified as Regime I. This regime was characterized by the natural mixing and combustion of fuel and oxidizer, forming a vertically elongated reaction zone due to buoyancy.

**Figure 4(b)** presents the results when operating two vacuum pumps, applying a coaxial aspiration velocity of  $-40$  cm/s. Under this condition, Regime II and Regime III alternated, depending on the fuel dilution ratio and nozzle exit mean velocity. When the fuel dilution ratio was high (1.0), combustion products such as CO<sub>2</sub> and soot were drawn downward, leading to the formation of Regime II across all nozzle exit mean velocities. Conversely, when the fuel dilution ratio dropped below 0.5 and nozzle exit mean velocity was reduced below 60 cm/s, Regime V, resembling a microgravity flame, was observed. As the nozzle exit mean velocity increased, the red flame zone transitioned into a ring-shaped structure around the flame, forming Regime III. With further coaxial aspiration velocity influence, the ring-shaped red zone shifted downward, leading to the reformation of Regime II.

**Figure 4(c)** illustrates the results when operating three vacuum pumps, applying a coaxial aspiration velocity of  $-60$  cm/s. Under this condition, when the fuel dilution ratio was below 0.4 and the nozzle exit mean velocity was below 20 cm/s, Regime V was predominantly observed, with minimal soot emission. However, as the nozzle exit mean velocity increased, the flame front began to split and was drawn downward, leading to the formation of Regime IV. During this transition, a blue flame region appeared along the central axis, while intermittent red flame formation was rapidly extracted. As the nozzle exit mean velocity increased further, the flame area expanded, ultimately transitioning into Regime II, similar to the observations in the  $-40$  cm/s condition.

The results observed in **Figures 4(a)** to **4(c)** indicate that the interactions among the three key variables were the primary cause of flame behavior variation. First, the strength of the coaxial aspiration velocity played a crucial role in determining the flame density and the direction of combustion product movement. In the absence of coaxial aspiration velocity ( $U_{co} = 0$  cm/s), the fuel and oxidizer naturally mixed, forming a stable diffusion flame structure (Regime I). However, when coaxial aspiration velocity was applied, combustion products such as CO<sub>2</sub> and soot were forcibly drawn downward, leading to flame structure

distortion and the emergence of new flame characteristics, such as red and blue flame zones.

The fuel dilution ratio influenced the properties of the combustion products. As the dilution ratio increased, soot formation was suppressed, whereas at lower dilution ratios, a larger quantity of combustion products was generated. This caused CO<sub>2</sub> and soot to move downward, resulting in structural changes in the flame.

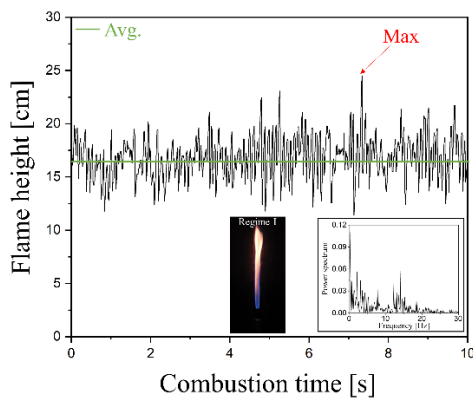
The nozzle exit mean velocity determined the structural transformation of the flame depending on its relative proportion to the coaxial aspiration velocity. At low nozzle exit mean velocities, the dominant suction flow drew the flame downward or confined it near the nozzle region. In contrast, at high nozzle exit mean velocities, the flame extended upward, indicating that nozzle velocity is a critical parameter influencing flame size.

In conclusion, the interactions among coaxial aspiration velocity, fuel dilution ratio, and nozzle exit mean velocity played a decisive role in determining flame structural stability and emission characteristics, as demonstrated by the distribution of different flame regimes.

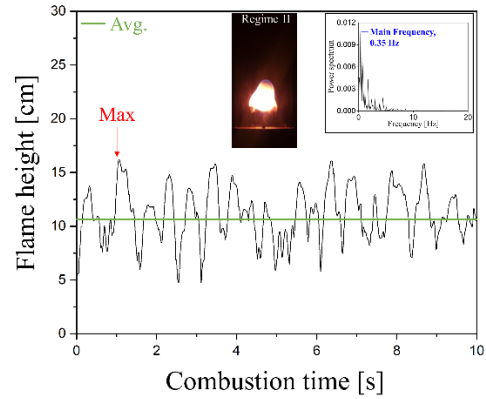
### 3.2 Analysis of Flame Height and Flame Frequency

Figures 5(a)-(e) present flame images representative of each Regime, along with flame height data derived using a MATLAB-based program. Additionally, the frequency characterization graphs obtained using FFT techniques are inserted in the upper or lower right of each graph based on the average flame height.

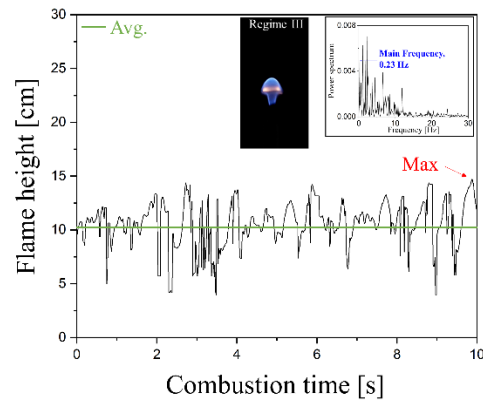
Regime I represents the baseline diffusion flame, exhibiting a typical diffusion flame structure. It is defined as a Natural Convection-Dominated Flame, where fuel injected from the nozzle mixes with atmospheric oxygen and combusts, showing a velocity distribution similar to the jet similarity solution. Figure 5(a)



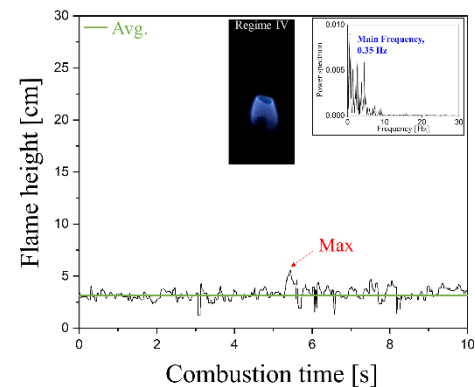
(a)



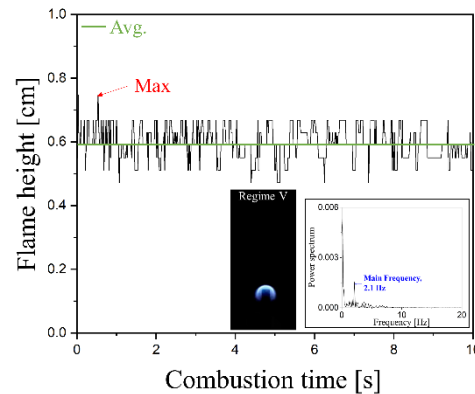
(b)



(c)



(d)



(e)

Figure 5: Flame height and flame frequency with various aspiration flow velocities

corresponds to the condition without coaxial suction flow, with a fuel dilution ratio of 0.5 and a nozzle exit mean velocity of 40 cm/s. The flame consists of a blue region near the nozzle and red luminescence in the upper section. After combustion, CO<sub>2</sub> and soot emissions are produced in the upper region, following a typical diffusion flame pattern, with a slender and elongated flame structure.

The maximum flame height was measured at 22.5 cm, while the average height was calculated to be 16.8 cm. FFT analysis was performed based on the average flame height to further characterize its frequency components. The specific flame frequencies observed result from intrinsic flame oscillations, turbulent interactions, and thermal and acoustic instabilities. Throughout the combustion process, flames exhibit resonant vibrations at specific frequencies, influenced by heat release, fuel-air mixing, and interactions with the flow field. These frequencies vary based on flame shape, fuel properties, and burner design conditions, including nozzle size and combustor length, reflecting the dynamic characteristics of the flame.

The primary frequency selection method typically involves choosing the highest amplitude frequency in the spectrum. However, in some cases, a lower amplitude frequency may hold greater physical or engineering significance. The selected primary frequency provides essential data for evaluating combustion system performance and optimizing design. It enables the assessment of system stability, interaction with combustor resonance frequencies, and quantification of heat release and flow characteristics. Such analyses serve as a foundation for optimizing combustion systems and mitigating instabilities, contributing to improved performance and reliability. In **Figure 5(a)**, the frequency analysis is displayed in the lower right section, and due to excessive noise in the spectrum, no primary frequency was selected.

Regime II exhibits a red flame zone, formed as CO<sub>2</sub> and soot are extracted downward by the operation of the vacuum pump. This structure is termed the Inside-Out Soot Flame. **Figure 5(b)** represents the condition where coaxial suction flow was induced at -40 cm/s using two vacuum pumps, with a fuel dilution ratio of 1.0 and a nozzle injection velocity of 140 cm/s. As fuel is injected from the nozzle, it diffuses under the influence of coaxial suction flow. The expanding red flame zones in both the upper and lower regions result from the accumulation of combustion products such as CO<sub>2</sub> and soot. The maximum flame height was measured at 16.2 cm, with an average height of 11.0 cm. The

primary frequency observed for this flame was 0.35 Hz.

Regime III exhibits a ring-like red flame zone surrounding the flame center, forming a mushroom-shaped structure, and is thus defined as the Mushroom-Shaped Flame. The coaxial aspiration velocity was -60 cm/s, with a fuel dilution ratio of 0.4 and a nozzle injection velocity of 60 cm/s. This flame structure closely resembles microgravity mushroom-shaped flames, which differ significantly from those observed under normal gravity conditions. Such formations arise due to the reduced influence of buoyancy-driven convection, allowing fuel and oxidizer to mix more uniformly, leading to a slowly expanding flame structure. The maximum flame height was measured at 14.6 cm, while the average height was 10.6 cm.

The frequency analysis revealed three distinct harmonic frequencies at 0.23 Hz, 1.05 Hz, and 2.34 Hz. These harmonics arise due to integer multiples of the fundamental frequency, a phenomenon typical of periodic signals. Such behavior is influenced by the nonlinear nature of the system, signal distortion, or resonance conditions. The fundamental frequency represents the primary oscillatory characteristic of the system, while harmonics contribute to signal complexity. Based on the frequency spectrum, 0.23 Hz was identified as the primary frequency, as it exhibited the most significant amplitude variation.

Regime IV features a circular blue flame front, forming a hollow central region, and is defined as the Cylindrical Flame. This flame was observed under a coaxial aspiration velocity of -60 cm/s, with a fuel dilution ratio of 0.4 and a nozzle injection velocity of 100 cm/s. This structure represents a stable cylindrical flame formed under strong co-flow influence, exhibiting unique combustion dynamics. In the upper section, fuel rapidly mixes with oxygen, producing a high-temperature combustion reaction, resulting in a blue flame region. The lower section gradually expands, allowing combustion gases to diffuse, leading to the formation of an exhaust gas zone.

In this flame, the lower section exhibits a color transition from blue to a faint reddish hue, indicating an area where combustion is nearly complete. This transition reflects the accumulation of exhaust gases, while the co-flow assists in the rapid expulsion of these gases. The coflowing air stabilizes the flame by ensuring a uniform downward flow from the upper to lower regions. The maximum flame height was measured at 5.8 cm, with an average height of 3.3 cm, and the primary frequency was 0.35 Hz. This frequency is attributed to the interaction between the fuel jet velocity and the negative flow velocity generated within the flow

field, leading to the formation of a vortex. The motion of this vortex affected the overall flame oscillation characteristics, establishing the dominant frequency in the spectrum.

Finally, Regime V represents a small spherical flame positioned at the nozzle tip, resembling a microgravity flame. This structure is defined as the Inhibited Natural Convection Flame. It was observed under a coaxial aspiration velocity of  $-40$  cm/s, with a fuel dilution ratio of 0.4 and a nozzle injection velocity of 40 cm/s. This hemispherical flame is characterized by a flat lower section and a slightly rounded upper portion. Such formations occur when the flame propagation speed and fuel supply rate are balanced, producing a stable combustion structure where the fuel concentration remains constant.

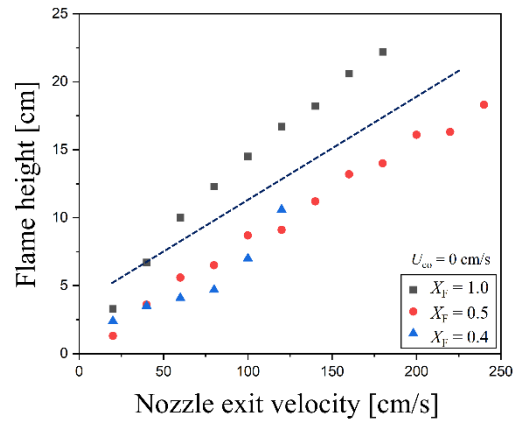
The maximum flame height was measured at 0.75 cm, while the average height was 0.6 cm. The primary frequency was identified as 2.1 Hz, rather than the initially observed frequency. Unlike the influence of external flow-induced vortex effects, this frequency resulted from internal flow field interactions within the flame itself. Due to the small flame size, surrounding vibrations had negligible impact on the flame dynamics. Instead, the dominant frequency arose from the internal combustion dynamics, making 2.1 Hz the primary frequency despite the presence of a higher initial amplitude frequency.

### 3.3 Characterization of Flame Dynamics

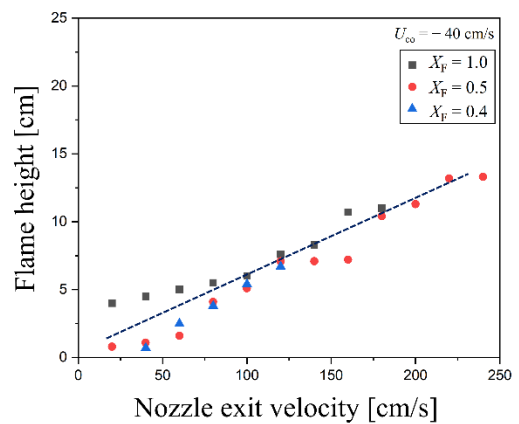
**Figures 6(a)-(c)** illustrate the relationship between nozzle exit velocity and flame height under varying coaxial aspiration velocities, providing a quantitative evaluation of flame height trends. In the case of **Figure 6(a)**, where no suction flow was applied, flame height increased linearly with nozzle exit velocity, although the slope and rate of increase differed depending on the conditions. At lower nozzle velocities, flame heights remained similar regardless of fuel dilution ratio ( $X_F$ ). However, as nozzle velocity increased,  $X_F = 1.0$  exhibited the steepest increase, followed by  $X_F = 0.5$  with a moderate increase, and  $X_F = 0.4$  with a gradual increase.

This result indicates that the fuel-oxidizer mixing ratio significantly influences flame formation and growth. In particular, at  $X_F = 1.0$ , where the fuel fraction was highest, the flame structure was optimized for combustion, making nozzle velocity a major factor in flame height variation. Conversely, at  $X_F = 0.4$ , the low mixing ratio limited flame formation, demonstrating that fuel dilution constraints influence flame development.

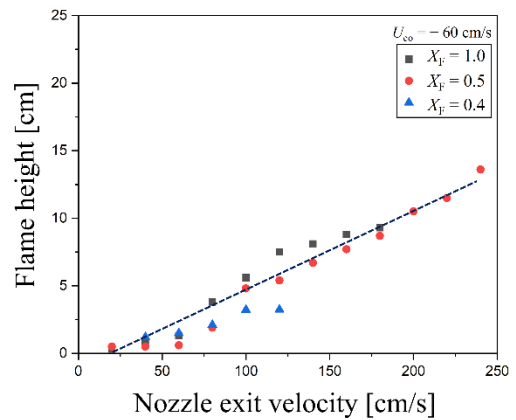
In Figures 6(b) and 6(c), where coaxial aspiration velocity was applied, flame height decreased overall for all  $X_F$  values. This



(a)



(b)



(c)

**Figure 6:** Average flame height by coaxial aspiration velocity, (a)  $U_{co} = 0$  cm/s, (b)  $U_{co} = -40$  cm/s, (c)  $U_{co} = -60$  cm/s

phenomenon can be attributed to changes in the flow field within the combustion zone due to suction, which restricted oxygen supply and fuel mixing conditions. Particularly, under a strong coaxial aspiration velocity of  $-60$  cm/s, the flow structure in the combustion region was altered, leading to further suppression of flame formation due to limited oxygen and fuel mixing. The

stronger suction also reduced the influence of nozzle velocity on flame height, further constraining the flame growth rate. Additionally, as coaxial aspiration velocity increased, the rate of change in flame height decreased, highlighting the significant impact of coaxial aspiration velocity on flame stability.

In this study, a nondimensional variable approach was used to quantitatively analyze the interactions between fuel dilution ratio, nozzle injection velocity, and coaxial aspiration velocity, allowing for a comparative assessment of flame height variations across different conditions. This approach enabled a systematic evaluation of relative flame height changes and identified correlations among the variables, as shown in **Figure 7(a)**. The x-axis variable ( $1/X_F$ ) represents the fuel dilution ratio, a constant, while the nondimensional combination of nozzle injection velocity and coaxial aspiration velocity accounts for fluid flow interactions. This variable allows for quantitative evaluation of the interplay between fuel dilution and flow characteristics, demonstrating that higher coaxial aspiration velocity limits flame formation.

The y-axis variable ( $L_{suc}/L_{default}$ ) represents the relative flame height change due to coaxial aspiration velocity, defined as the flame height under suction conditions normalized by the baseline flame height (without coaxial aspiration velocity). The analysis results showed a linear relationship between these two nondimensional variables, expressed as:

$$L_{suc}/L_{default} = 0.21 \frac{(U_f - U_{co})}{X_F \cdot U_f} + 0.34 \quad (1)$$

This equation confirms that the combined effects of fuel dilution ratio, nozzle velocity, and coaxial aspiration velocity play a critical role in determining the relative rate of flame height change and that their interactions can be quantitatively assessed. Under the  $-60$  cm/s suction condition, flame height remained relatively stable and was less affected by coaxial aspiration velocity. This is attributed to higher nozzle velocity increasing inertial force, which enhanced flame stability. Conversely, under the  $40$  cm/s nozzle condition, flame height was generally lower and more sensitive to coaxial aspiration velocity. This analysis systematically evaluates the interaction of fuel dilution ratio, nozzle velocity, and coaxial aspiration velocity on flame height and provides fundamental data for combustion system design.

Furthermore, the nondimensional variable approach defined in this study facilitates the generalization of flame height behavior across different conditions and provides design guidelines for

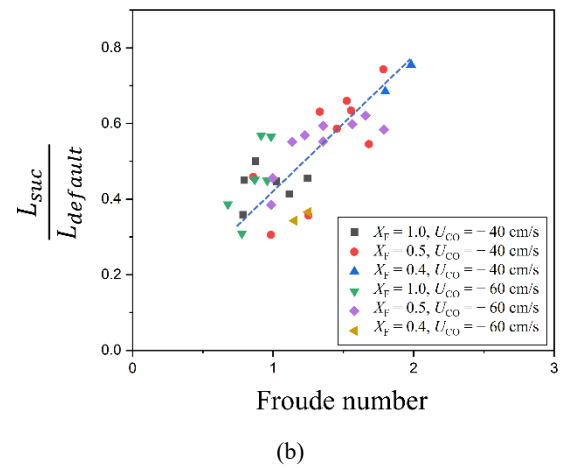
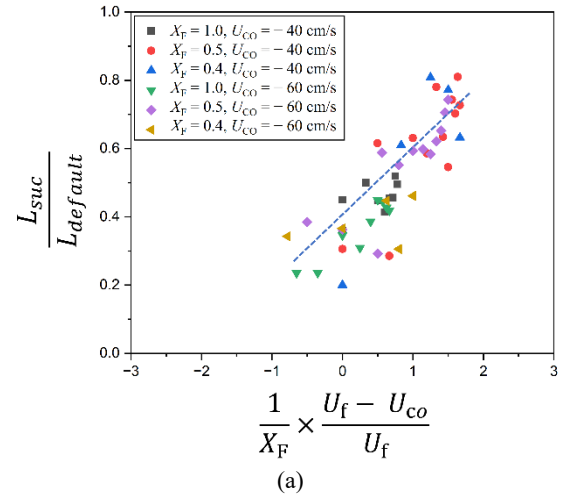


**Figure 7:** Characterization of flame length ratio and non dimensional (a) mixture condition, (b) Froude number

maintaining combustion stability.

Additionally, the Froude number ( $Fr$ ) was utilized to nondimensionalize fuel dilution ratio, nozzle injection velocity, and coaxial aspiration velocity, allowing for a quantitative assessment of relative flame height changes. This approach enabled comparisons across experimental conditions, ensuring a generalized analysis of flame characteristics. The Froude number, which represents the ratio of inertial force to gravitational force in fluid flow, is defined as follows:

- In the case of  $Fr > 1$ , inertial forces dominate the flame flow field over gravitational forces.
- In the case of  $Fr < 1$ , gravitational forces are dominant in the flame flow field.

Based on this principle, **Figure 7(b)** plots the ratio of flame height under suction conditions to the flame height without coaxial aspiration velocity (y-axis) against the Froude number (x-axis).

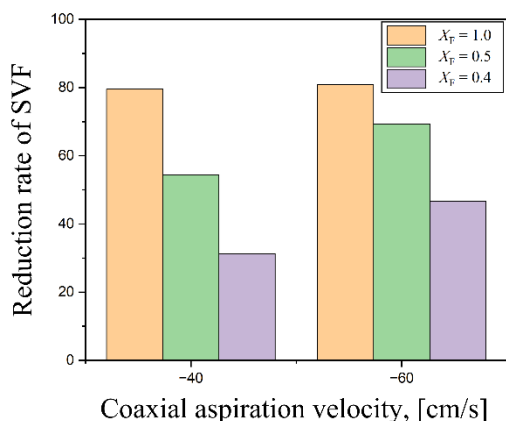


**Figure 8:** Reduction rate of soot volume fraction

As suction flow increasingly dominated the flow field, flame height decreased, and the Froude number fell below 1, indicating that gravitational forces played a major role in flame dynamics. Conversely, when coaxial aspiration velocity was relatively weak compared to nozzle exit velocity, flame height reduction was significantly lower, and the Froude number exceeded 1, highlighting a flow field strongly influenced by jet velocity and buoyancy effects.

Finally, to quantitatively evaluate the effects of coaxial aspiration velocity and fuel dilution ratio on the reduction of soot volume fraction (SVF), MATLAB-based flame image analysis was conducted. This analysis not only determined the SVF reduction rate under different experimental conditions but also clarified the interaction between coaxial aspiration velocity and fuel dilution ratio in soot formation. The flame image data were processed by converting captured frames into an analyzable format, enabling soot quantification.

Using MATLAB, the red zone in flame images was filtered to extract soot formation regions, and a threshold value was set to isolate soot-dominated pixels. The analysis results, shown in **Figure 8**, revealed that maximum soot reduction (up to 80%) was achieved under the condition of  $-60$  cm/s coaxial aspiration velocity and  $X_F = 1.0$ , compared to the non-suction baseline condition.

#### 4. Conclusion

This study serves as a fundamental investigation into a novel suction-based method for controlling carbon-based emissions, including  $\text{CO}_2$  and soot, generated during the combustion of methane fuel, which is widely used in industrial, commercial, and residential sectors. To experimentally verify and analyze the flow

paths of  $\text{CO}_2$  and soot under suction flow conditions within a methane flame flow field, a coaxial burner equipped with a vacuum pump-based suction system was constructed. To create various flame flow structures, an inert gas (nitrogen) was added at a fixed dilution ratio, and the nozzle injection velocity was adjusted to define different fuel mixtures. Through this study, the following results were obtained:

1. An experimental study was conducted to guide the extraction of various combustion emissions generated in methane-fueled burners into a designated space. The coaxial burner was utilized as a combustion system, enabling the observation and analysis of flame behavior variations under different suction velocities.
2. The flame structure and shape varied with suction velocity, leading to the classification of five distinct flame regimes. Notably, when a strong negative coaxial flow was applied, a flame resembling microgravity conditions was observed, along with a diffusion-dominated blue flame that exhibited no visible soot particles.
3. The application of suction flow to the coaxial burner resulted in a reduction of  $\text{CO}_2$  and soot particles. Specifically, under the  $-60$  cm/s suction velocity condition, the soot reduction efficiency reached up to 80%, demonstrating excellent performance in emission control.
4. The study successfully characterized and predicted flame length variations based on combustor operating conditions, including fuel-nitrogen dilution ratio, nozzle injection velocity, and suction velocity. These findings suggest that the results can be applied to industrial combustion systems, providing controllable parameters for optimizing combustor design.

Through this study, an effective method was proposed for regulating flame length and emissions by diluting methane with nitrogen, as outlined in the four key findings. This approach not only enhances fuel efficiency but also contributes to minimizing carbon emissions, offering potential applications in the development of environmentally friendly combustion systems.

#### Acknowledgement

This work was supported by Basic Science Research Program through the National Research Foundation of Korea (NRF) funded by the Ministry of Education (No.2021R111A3061305).

## Author Contributions

Conceptualization, J. W. Kim and S. H. Yoon; Methodology, J. W. Kim and J. Park; Software, J. W. Kim and J. Park; Validation, J. W. Kim and S. H. Yoon; Formal Analysis, J. W. Kim and J. Park; Investigation, J. W. Kim and J. Park; Resources, First Author; Data Curation, J. W. Kim; Writing—Original Draft Preparation, J. W. Kim and J. Park; Writing—Review & Editing, S. H. Yoon; Visualization, J. W. Kim; Supervision, S. H. Yoon; Project Administration, S. H. Yoon; Funding Acquisition, S. H. Yoon.

## References

- [1] UNFCCC, United Nations Framework Convention on Climate Change, <https://unfccc.int/resource/docs/convkp/convening.pdf>, Accessed December 30, 2024.
- [2] UNFCCC, KYOTO Protocol to the United Nations Framework Convention on Climate Change, United Nations, 1998.
- [3] C. Acar, A. Beskese, and G. T. Temur, “Sustainability analysis of different hydrogen production options using hesitant fuzzy AHP,” *International Journal of Hydrogen Energy*, vol. 43, pp. 18059-18076, 2018.
- [4] Climate Change Conference, COP26, The Glasgow Climate Pact. UN Climate Change Conference, Glasgow, UK, 2021. Available: <https://ukcop26.org/wp-content/uploads/2021/11/COP26-Presidency-Outcomes-The-Climate-Pact.pdf>.
- [5] H. H. Cho, V. Strezov, and T. J. Evans, “A review on global warming potential, challenges and opportunities of renewable hydrogen production technologies,” *Sustainable Materials and Technologies*, vol. 35, e00567, 2023.
- [6] UNFCCC, Paris Agreement, [https://unfccc.int/sites/default/files/english\\_paris\\_agreement.pdf](https://unfccc.int/sites/default/files/english_paris_agreement.pdf), Accessed December 30, 2024.
- [7] J. Rogelj, G. Luderer, R. C. Pietzcker, E. Kriegler, M. Schafer, V. Krey, and K. Riahi, “Energy system transformations for limiting end-of-century warming to below 1.5°C,” *Nature Climate Change*, vol. 5, pp. 519-527, 2015.
- [8] IPCC, “Summary for Policymakers. In: Masson-Delmotte *et al.*, editors. *Global warming of 1.5°C: An IPCC Special Report On The Impacts Of Global Warming Of 1.5°C Above Pre-Industrial Levels And Related Global Greenhouse Gas Emission Pathways, In The Context Of Strengthening The Global Response To The Threat Of Climate Change.*” [https://www.ipcc.ch/site/assets/uploads/sites/2/2018/07/SR15\\_SPM\\_High\\_Res.pdf](https://www.ipcc.ch/site/assets/uploads/sites/2/2018/07/SR15_SPM_High_Res.pdf), Accessed December 30, 2024.
- [9] Government of Korea, 2050 Carbon Neutral Strategy of the Republic of Korea: Towards a sustainable and green society (In Korean), 2020. Available: [https://unfccc.int/sites/default/files/resource/LTS1\\_RKorea.pdf](https://unfccc.int/sites/default/files/resource/LTS1_RKorea.pdf).
- [10] Ministry of Foreign Affairs of the People’s Republic of China, “Statement by H.E. Xi Jinping President of the People’s Republic of China at the General Debate of the 75th Session of The United Nations General Assembly,” 2021. Available: [https://www.fmprc.gov.cn/mfa\\_eng/zxxx662805/t1817098.shtml](https://www.fmprc.gov.cn/mfa_eng/zxxx662805/t1817098.shtml).
- [11] MOTIE, Ministry of Trade industry and Energy, Green Growth Strategy Through Achieving Carbon Neutrality in 2050, 2021 (in Korean). Available: [https://www.meti.go.jp/english/policy/energy\\_environment/global\\_warming/ggs2050/pdf/ggs\\_full\\_en1013.pdf](https://www.meti.go.jp/english/policy/energy_environment/global_warming/ggs2050/pdf/ggs_full_en1013.pdf).
- [12] IEA, CO<sub>2</sub> Emissions in 2022, [https://iea.blob.core.windows.net/assets/3c8fa115-35c4-4474-b237-1b00424c8844/CO2\\_Emissionsin2022.pdf](https://iea.blob.core.windows.net/assets/3c8fa115-35c4-4474-b237-1b00424c8844/CO2_Emissionsin2022.pdf), Accessed December 30, 2024.
- [13] X. Zhang, N. P. Myhrvold, Z. Hausfather, and K. Caldeira, “Climate benefits of natural gas as a bridge fuel and potential delay of near-zero energy systems,” *Applied Energy*, vol. 167, pp. 317-322, 2016.
- [14] M. Levi, “Climate consequences of natural gas as a bridge fuel,” *Climatic Change*, vol. 118, pp. 609-623, 2013.
- [15] IPCC, *Climate Change 2018: The Physical Science Basis*, Cambridge University Press: Cambridge, UK, 2018.
- [16] R. G. Derwent, “Global Warming Potential (GWP) for Methane: Monte Carlo Analysis of the Uncertainties in Global Tropospheric Model Predictions,” *Atmosphere*, vol. 11, 486, 2020.
- [17] IPCC, 7.SM Chapter7: The Earth’s Energy Budget, Climate Feedbacks, and Climate Sensitivity-Supplementary Material, IPCC AR6 WGI, 2022.
- [18] H. Y. Seo, H. R. Heo, and Y. H. Yeon, “Methane Reduction Strategies and Regulations in South Korea: Current Issues and Policy Recommendations,” *Solutions for Our Climate*, 2023.
- [19] KOSIS, Trends in power generation (2015~2023), [https://kosis.kr/statHtml/statHtml.do?orgId=310&tblId=DT\\_31002N\\_A001&vw\\_cd=MT\\_ZTITLE&list\\_id=U\\_15&scrId=&seqNo=&lang\\_mode=ko&obj\\_var\\_id=&itm\\_id=&conn\\_path=](https://kosis.kr/statHtml/statHtml.do?orgId=310&tblId=DT_31002N_A001&vw_cd=MT_ZTITLE&list_id=U_15&scrId=&seqNo=&lang_mode=ko&obj_var_id=&itm_id=&conn_path=)

MT\_ZTITLE&path=%252FstatisticsList%252FstatisticsListIndex.do, Accessed December 30, 2024.

- [20] E. D. Lebel, C. J. Finnegan, Z. Ouyang, and R. B. Jackson, “Methane and NO<sub>x</sub> emissions from natural gas stoves, cooktops, and ovens in residential homes,” *Environmental Science & Technology*, vol. 56, pp. 2529-2539, 2022.
- [21] KATS, *Household and Similar Electrical Appliances – Safety Part 2-31: Particular Requirements for Range Hoods and Other Cooking Fume Extractors*, 2022.
- [22] S. H. Yoon, J. Park, O. B. Kwon, J. H. Yun, and S. I. Keel, “Self-excitation in laminar lifted free-jet propane flames diluted with nitrogen,” *Combustion and Flame*, vol. 158, pp. 1960-1969, 2011.